Supplementary Information

Self-Adaptive Interfaces via Electrochemical Reconstruction Enabling Efficient PV-PEC Water Splitting

*Shaohua Xie[a,b], Xiangrong Li[a], Youtian Mo[c], Wenliang Wang[a,] * and Guoqiang Li[a,] **

[a] State Key Laboratory of Luminescent Materials and Devices, School of Materials Science and Engineering, South China University of Technology, Guangzhou 510640, China

[b] State Key Laboratory of Silicon and Advanced Semiconductor Materials, Department of Polymer Science and Engineering, Zhejiang University, Hangzhou 310058, China

[c] School of Chemistry and Materials Science, Guangdong University of Education, Guangzhou 510303, China

[*] Corresponding author, E-mail: wenliangwang@scut.edu.cn and msgli@scut.edu.cn

Experimental Section

Synthesis of InN NRs. The InN NRs has been prepared via an in-situ growth molecular beam epitaxy (MBE) technology on Si substrate.[1] Under the beam equivalent pressure (BEP) of 3.5×10^{7} Torr for indium, with a forward plasma power of 400 W and a nitrogen flow rate of 2.00 sccm, the growth was carried out at 400 °C for 2 hours, respectively.

Synthesis of InN NRs/PM6 photocathode. The PM6 chlorobenzene solutions with mass concentrations of 5, 10, and 20 mg/mL were prepared. A drop of solution about 15 μL was added onto the InN NRs, followed by annealing at 100°C for 10 minutes. The samples were named as InN/PM6-5, InN/PM6-10, and InN/PM6-20, respectively. Furthermore, under the condition of a fixed speed of 4000 rpm for 30 seconds, PM6 film was spin coated and annealed at 100 ℃ for 10 minutes. The resulting photocathodes were designated InN/PM6-5', InN/PM6-10', and InN/PM6-20', respectively.

Synthesis of InN NRs/PM6/Ni LDH photocathode. The Ni LDH was electrochemically deposited onto InN/PM6 photocathode. The as-prepared samples were used as working electrodes, platinum plate electrodes as counter electrodes, and Ag/AgCl electrodes as reference electrodes, with an electrodeposition contact electrolyte area of 0.2 cm^2. The deposition was carried out in a 0.15 M $NiSO_4 \cdot 6H_2O$ electrolyte. Applying a constant current density of 10 mA/cm^2 for varying durations of 30, 60, 90, and 120 seconds, these samples were named as InN/PM6/Ni LDH-30, InN/PM6/Ni LDH-60, InN/PM6/Ni LDH-90, and InN/PM6/Ni LDH-120, reflecting the respective deposition times.

Synthesis of InN NRs/PM6/Ni-P photocathode. The synthesis of InN/PM6/Ni-P photocathode followed a procedure akin to that of InN/PM6/Ni LDH, with the distinction of incorporating P from $NaH_2PO_2\ H_2O$. The molar ratio of the added P source to $NiSO_4 \cdot 6H_2O$ was varied to 5%, 10%, 15%, and 20%. The synthesized samples were correspondingly named InN/PM6/Ni-P-5%, InN/PM6/Ni-P-10%, InN/PM6/Ni-P-15%, and InN/PM6/Ni-P-20%, reflective of their respective P content percentages.

Synthesis of GaAs/CNTGO/WO_3 heterojunction solar cells. According to the previously reported procedure[2], GO with different thicknesses was prepared using cyclic voltammetry by the three-electrode method, and a 15nm thick WO_3 layer was deposited by evaporation to prepare the heterojunction solar cells.

Synthesis of PV-PEC system. Under unbiased conditions, a two-electrode PV-PEC system was configured by coupling the GaAs/CNTGO/WO_3 heterojunction solar cell as photoanode with InN/PM6/Ni-based catalyst photocathode.

Materials Characterization. The morphology and structural information were characterized by field emission scanning electron microscopy (FE-SEM, Hitachi SU-8020) and high-resolution transmission electron microscopy (HRTEM, JEOL 3000F, FEI). The crystalline structure analysis of samples was verified through X-ray diffraction (XRD, Rigaku, Miniflex 600). The chemical state of the elements was investigated using the X-ray photoelectron spectroscopy (XPS, JEOL, JPS-9200). The paramagnetic species and defects in the samples were measured by the Electron Paramagnetic Resonance (EPR, Bruker A300). The functional group structure of the samples was characterization using fourier transform infrared spectroscopy (FTIR, Brucker TENSOR27). The optical properties of these samples were assessed using a UV-Vis spectrophotometer (Perkin Elmer, Lambda 950) and a fluorescence spectrophotometer (FLS 1000). The hydrogen produced during the reactions were analyzed using the gas chromatograph (GC-9560). The J-V characteristics of solar cells were measured under AM 1.5G illumination (100 mW cm^{-2}) using a class 3A solar simulator (Oriel, Newport) and a Keithley 2400 source meter.

PEC Measurements. All electrochemical measurements were performed on the electrochemical workstation (CHI 760E, CH Instruments Inc.), and performance data were averaged from three sample tests. The as-prepared photocathodes were used as the working electrode, the Pt sheets was used as the counter electrode, and the Ag/AgCl electrode was applied as the reference electrode. All the area of electrodes are 0.20 cm^2. Besides, the photocathodes were tested in 0.1 M KOH (pH = 13) under irradiation. The applied potential is generally converted to a reversible hydrogen electrode (RHE) scale according to the Nernst equation, which can be obtained from the following equation:[3]

$$E = \mathrm{E}_{app} + E^{0}_{\mathrm{Ag/AgCl}} + 0.059 \times \mathrm{pH} \quad (1)$$

Where the standard electrode potential of $E^{0}_{\mathrm{Ag/AgCl}}$ is 0.192 V, respectively.

The PEC performance of all photocathodes was assessed by calculating the ABPE using the subsequent formula:[4]

$$ABPE(\%) = |J_{ph} \times V_{app}|/P \times 100\% \quad (2)$$

$$ABPE(\%) = |J_{ph} \times (1.23 - V_{app})|/P \times 100\% \quad (3)$$

where J_{ph}, V_{app}, P are the photocurrent density, applied potential, and the incident light intensity, respectively. For the HER, the ABPE is calculated using Equation (2); for the OER, Equation (3) is employed.

Based on the long-term J-t curves, the STH efficiency can be determined using the measured photocurrent and the Faradaic efficiency for hydrogen production with the following equation:[5]

$$STH = J_{ph} \times 1.23 \times \eta_F/P \times 100\% \quad (4)$$

where J_{ph} is the photocurrent density at steady state, η_F is the Faradaic efficiency of the photocathodes, which is nearby to 1.

Turnover frequency (TOF) refers to the number of product molecules converted per active site per unit time on an electrode material. This parameter quantifies the reaction capability of individual catalytic sites, reflecting the intrinsic activity of the material. As a critical metric for evaluating catalyst reaction kinetics, a higher TOF value indicates stronger inherent catalytic activity. TOF can be calculated using Equation:[6]

$$TOF = J \times A/(m \times n \times F) \quad (5)$$

where J represents the current density at a specific potential, A is the area of electrodes, n is the number of moles of active sites, F is the Faraday constant (96485 C mol^{-1}), m represents the number of electrons transferred corresponding to the generation of the target product (when the reaction is HER, m is 2; When the reaction is OER, m is 4), respectively.

To evaluate the true catalytic activity of materials, it is often necessary to analyze their actual surface area involved in electrochemical catalytic reactions. The electrochemically active surface area (ECSA) can be obtained according to the following equation:[7]

$$ECSA = C_{dl}/A \times C_S \quad (6)$$

where C_{dl} is the double layer capacitance of electrodes, C_S is the Standard specific capacitance, usually taken as 0.040 mF/cm^2, A is the area of electrodes, respectively.

The transient decay time was analyze using the logarithmic plot of the parameter D with the following equation:[8]

$$D = (J_t - J_s)/(J_m - J_s) \quad (7)$$

where J_t is the photocurrent density, J_s is the photocurrent density at steady state, J_m is the photocurrent density spike under light. The transient decay time can be defined as the time when ln D = -1.

The electrochemical impedance spectroscopy (EIS) tests were performed at 0 V_{RHE}. The long-term stability and hydrogen evolution were measured under illumination. The Mott-Schottky (M-S) plots for these photocathodes were recorded at a frequency of 5000 Hz under dark conditions. The assessment of the flat band potential (V_{fb}) is essential for understanding the electron transfer among in the semiconductor. This value can be derived using the subsequent equation:[9]

$$1/C_S^{\,2} = 2/(\varepsilon_r\, \varepsilon_0\, A^2 q\, N_d)\, (V_{app} - V_{fb} - kT/q) \quad (8)$$

where C_S, ε_r, ε_0, V_{app} are represented the capacitance at the interface between the semiconductor and the electrolyte, the relative dielectric constant of the semiconductor, the permittivity of the vacuum, and the applied potential, respectively.

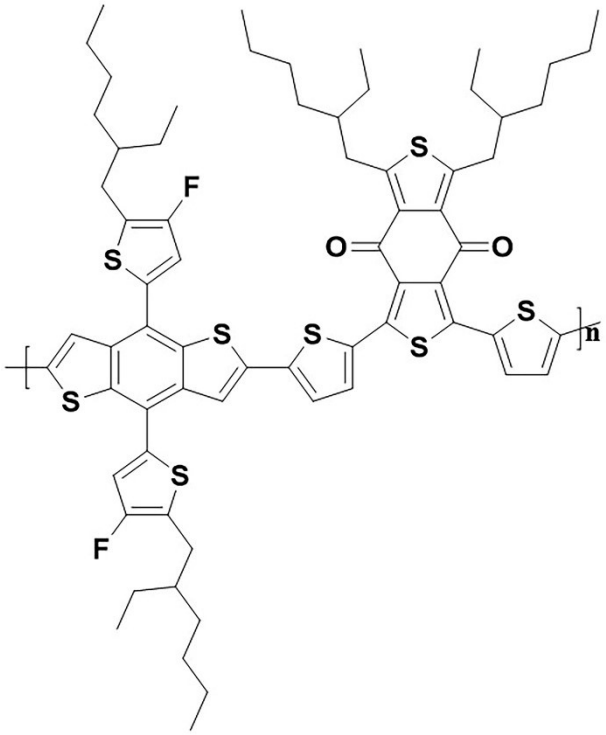

Figure S1. The chemical structure of PM6.

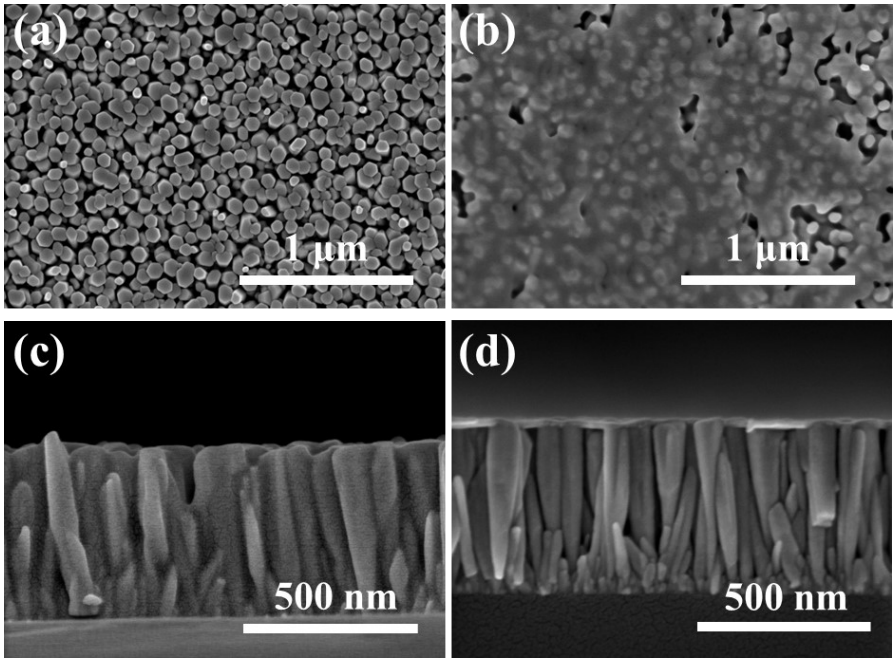

Figure S2. Top view SEM image of (a) InN NRs and (b) InN/PM6 hybrid (Scale bar: 1 μm). Cross-section SEM images of (c) InN NRs and (d) InN/PM6 hybrid (Scale bar: 500 nm).

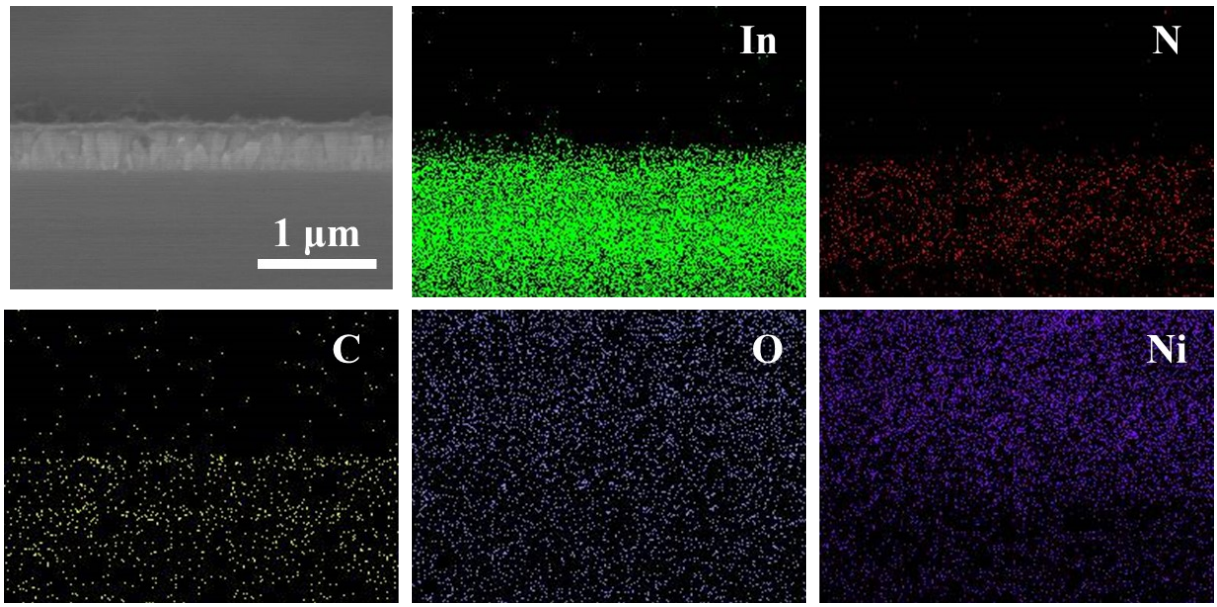

Figure S3. Cross-sectional SEM images and the corresponding elemental mapping images of the InN/PM6/Ni LDH photoelectrode.

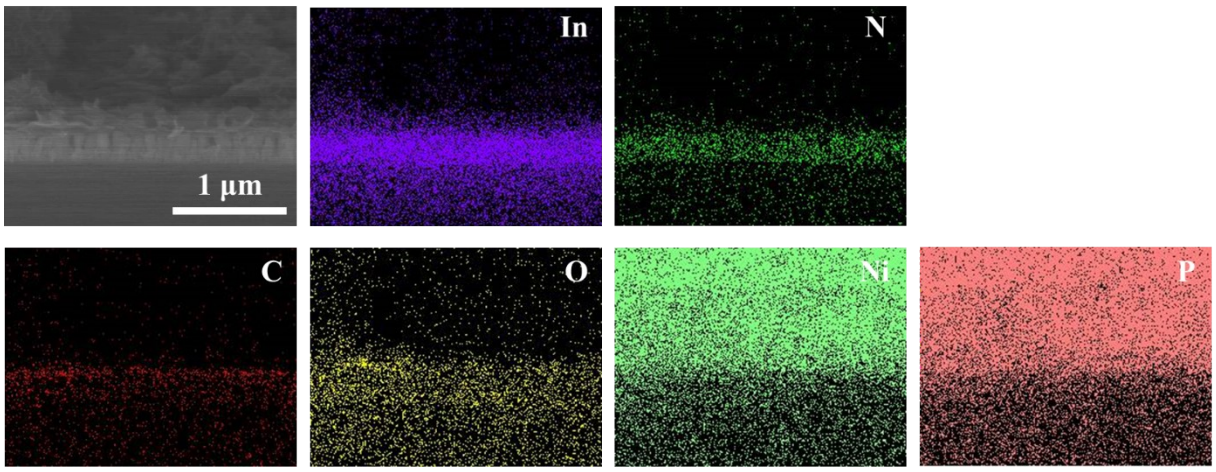

Figure S4. Cross-sectional SEM images and the corresponding elemental mapping images of the InN/PM6/Ni-P photoelectrode.

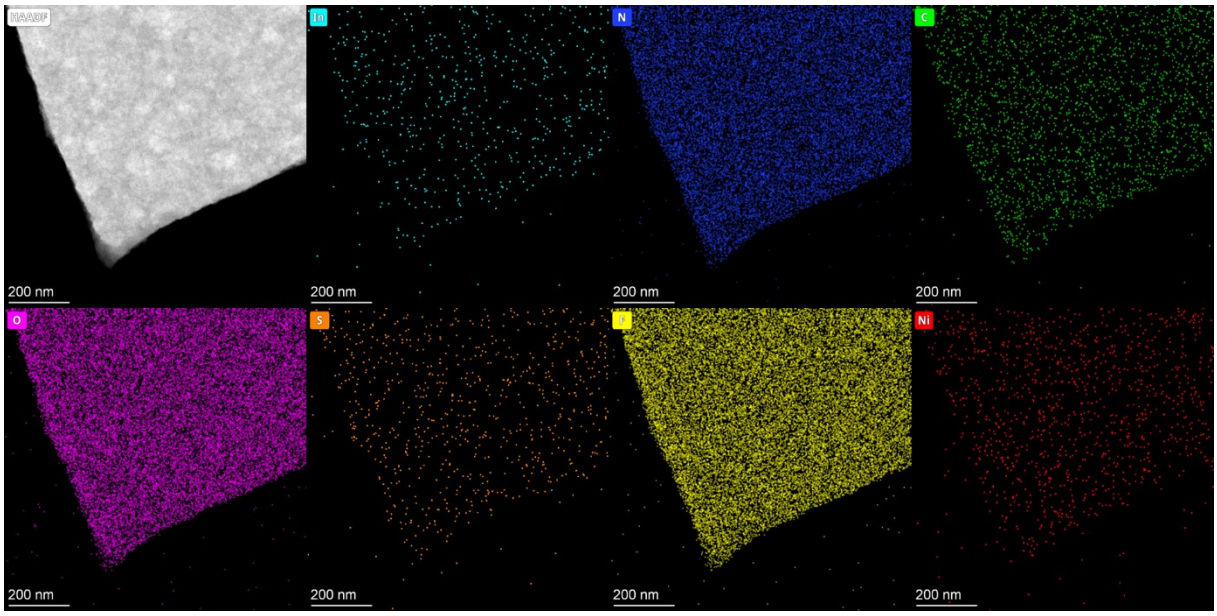

Figure S5. Top view HAADF-STEM images and the corresponding elemental mapping images of the InN/PM6/Ni LDH photoelectrode.

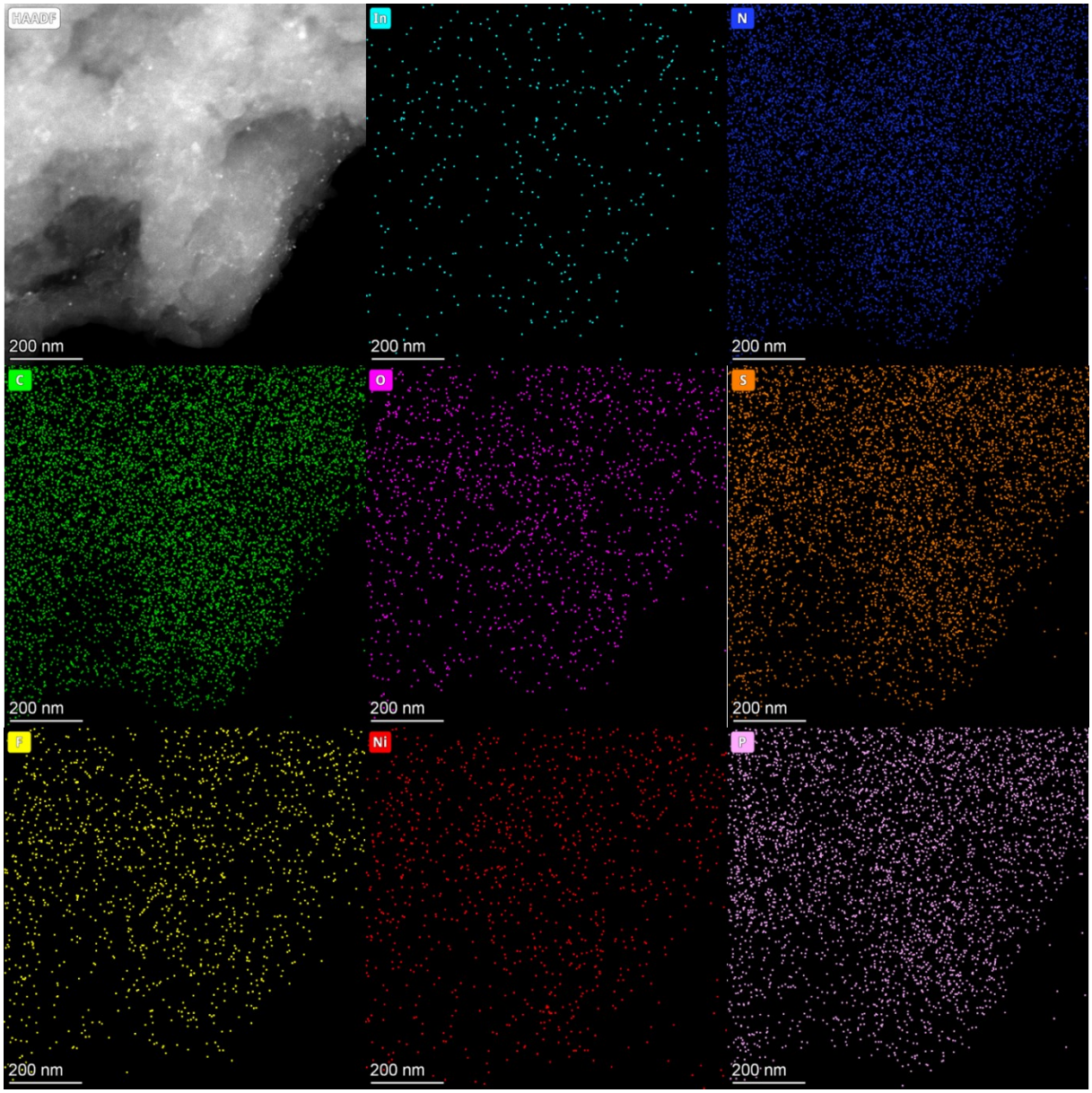

Figure S6. Top view HAADF-STEM images and the corresponding elemental mapping images of the InN/PM6/Ni-P photoelectrode.

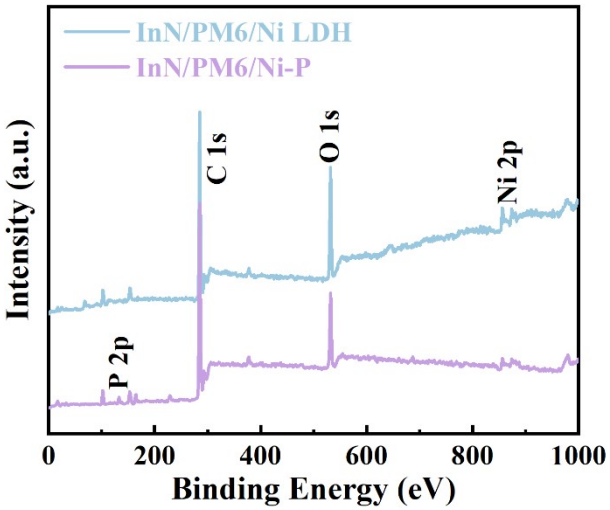

Figure S7. The XPS full spectrum of InN/PM6/Ni LDH and InN/PM6/Ni-P.

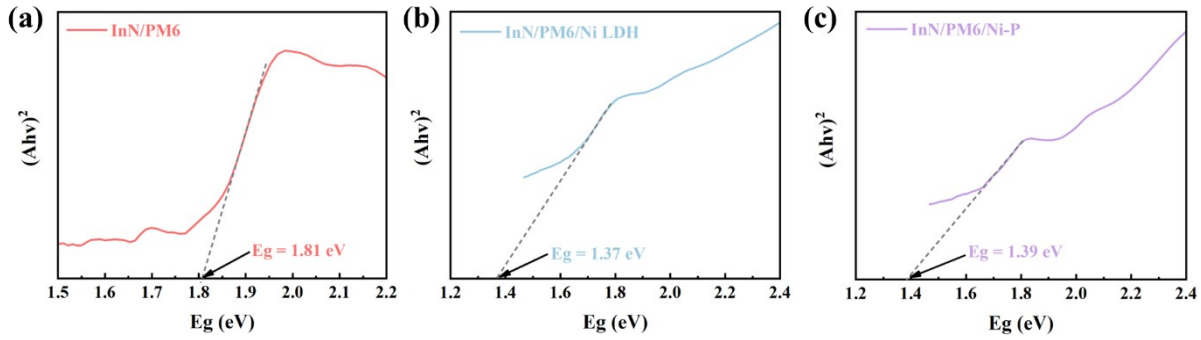

Figure S8. Tauc plots of the Kubelka-Munk function versus photon energy (Eg) of (a) InN/PM6, (b) InN/PM6/Ni LDH, and (c) InN/PM6/Ni-P.

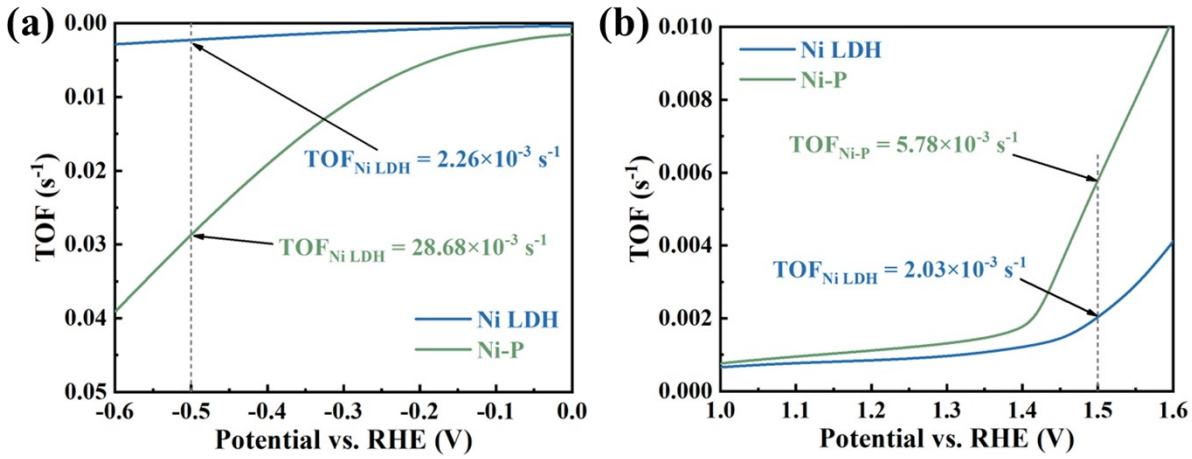

Figure S9. TOF values of Ni LDH and Ni-P for (a) HER and (b) OER.

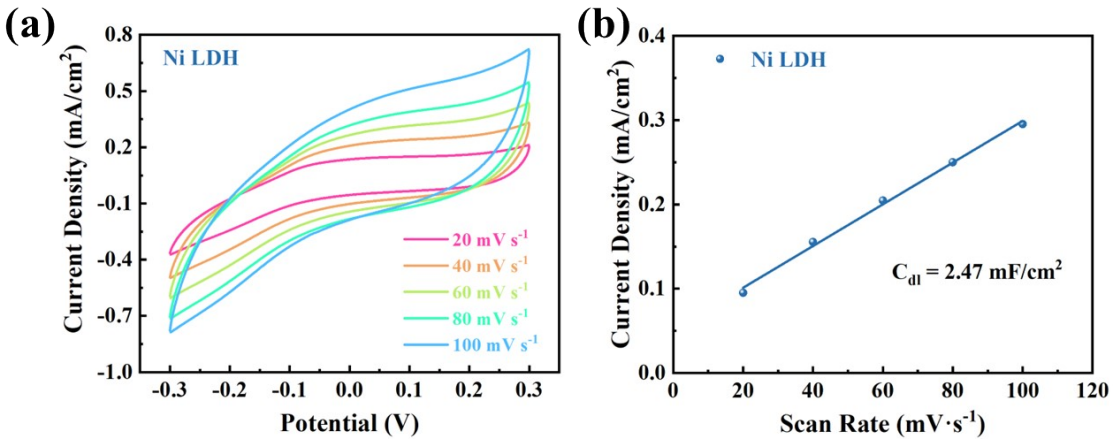

Figure S10. (a) CV curves at different scan rates and (b) C_{dl} value calculated from CV plots at different scan rates of Ni LDH.

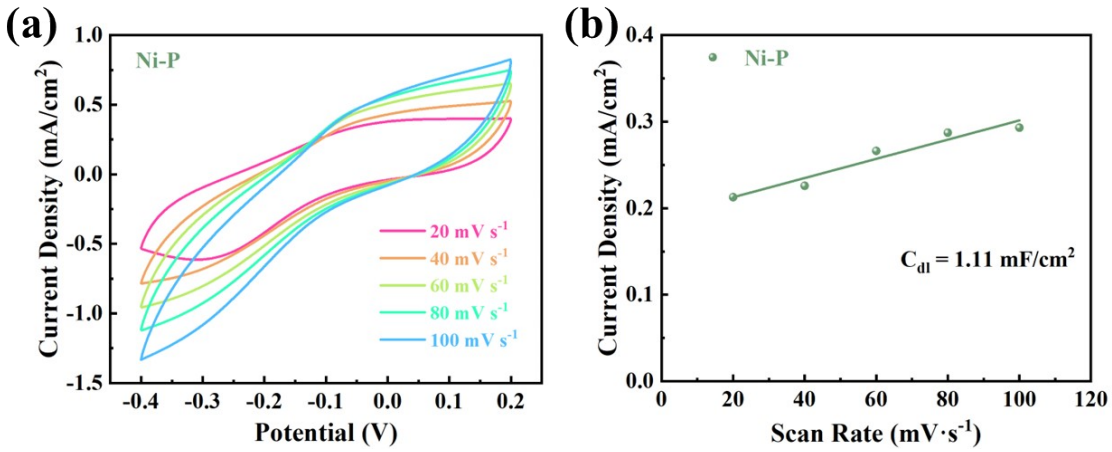

Figure S11. (a) CV curves at different scan rates and (b) C_{dl} value calculated from CV plots at different scan rates of Ni-P.

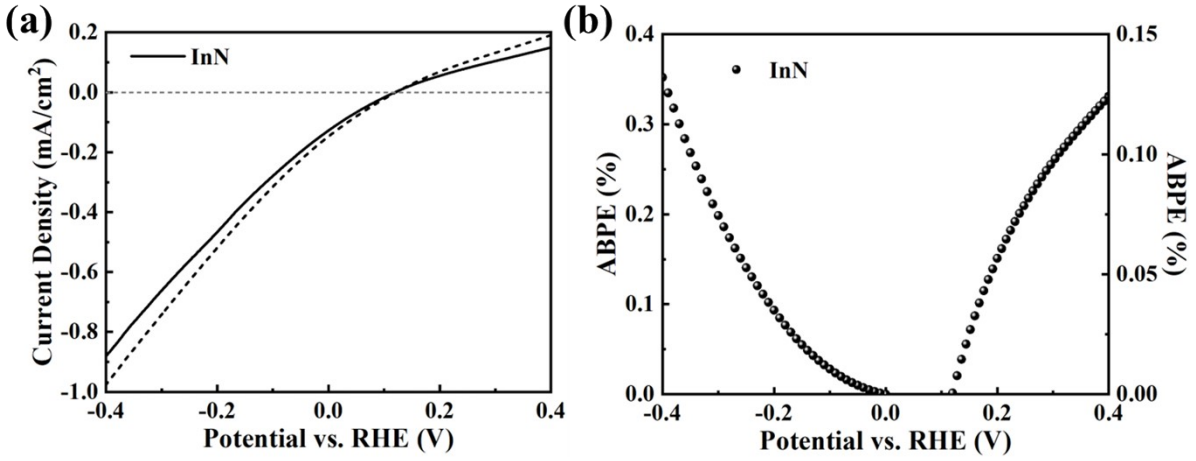

Figure S12. The (a) LSV curves, (b) ABPE curves of InN photoelectrode.

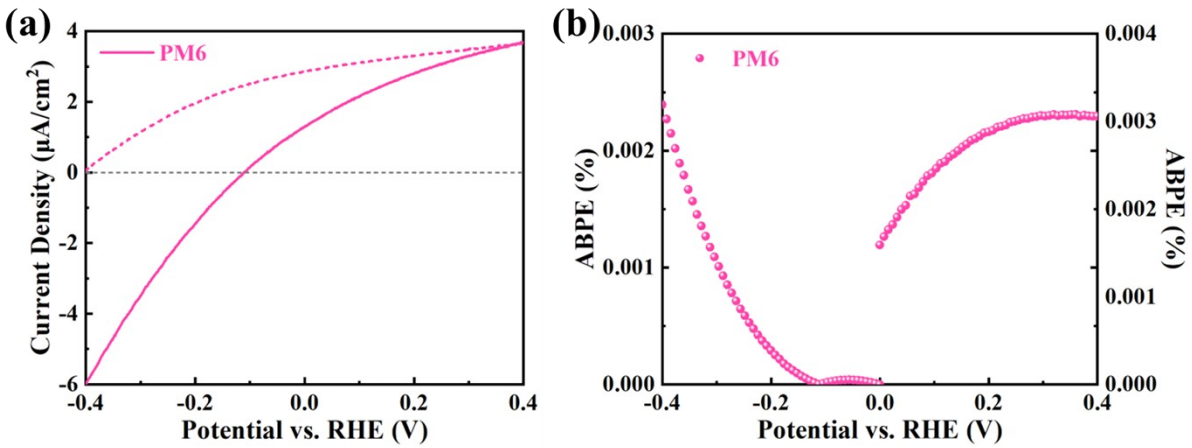

Figure S13. The (a) LSV curves, (b) ABPE curves of PM6 photoelectrode.

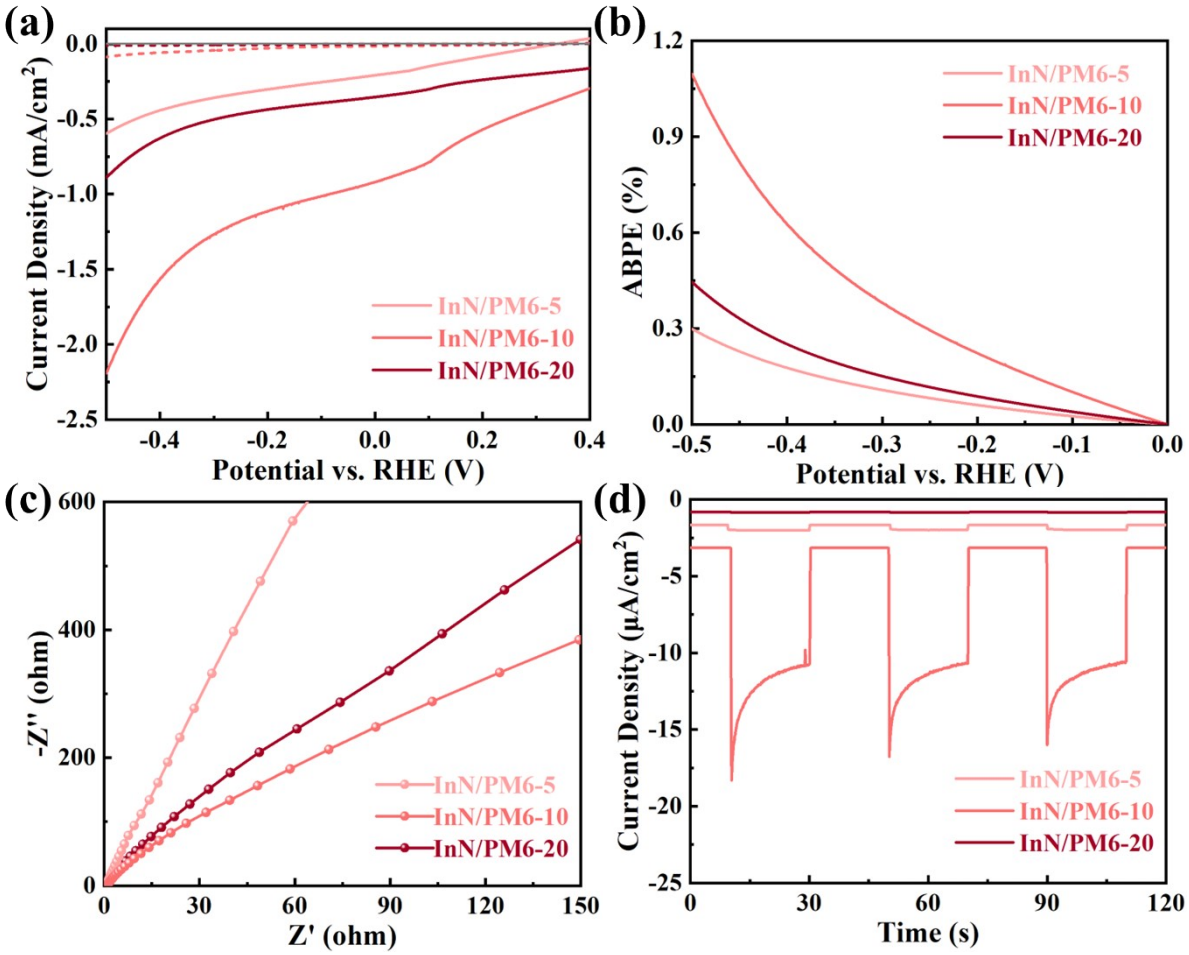

Figure S14. The (a) LSV curves, (b) ABPE curves, (c) EIS spectra, and (d) chopping J-t curves of InN/PM6 photocathodes with varying mass concentrations.

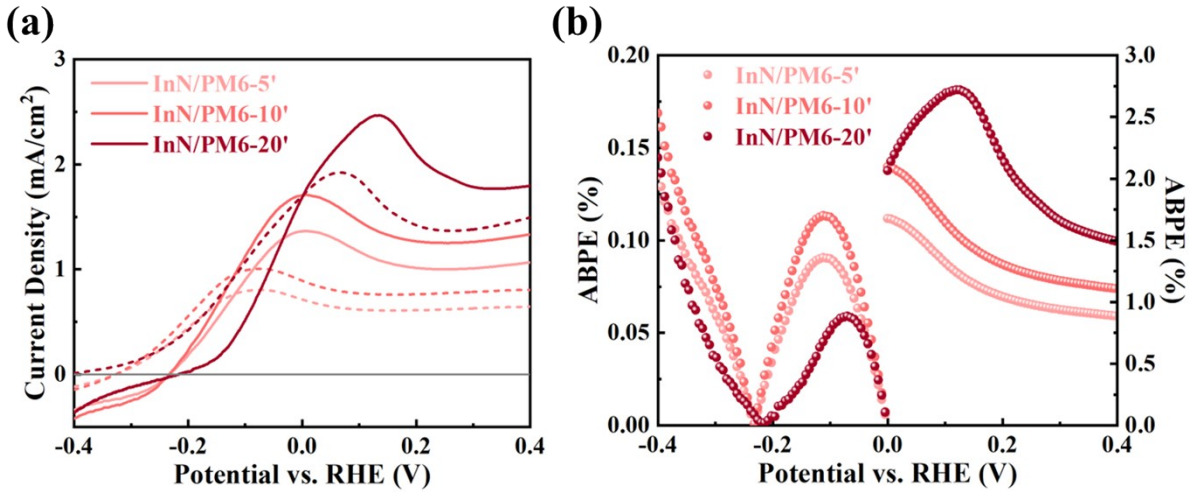

Figure S15. The (a) LSV curves, (b) ABPE curves of InN/PM6 photoelectrodes with varying mass concentrations spin coated at 4000 rpm.

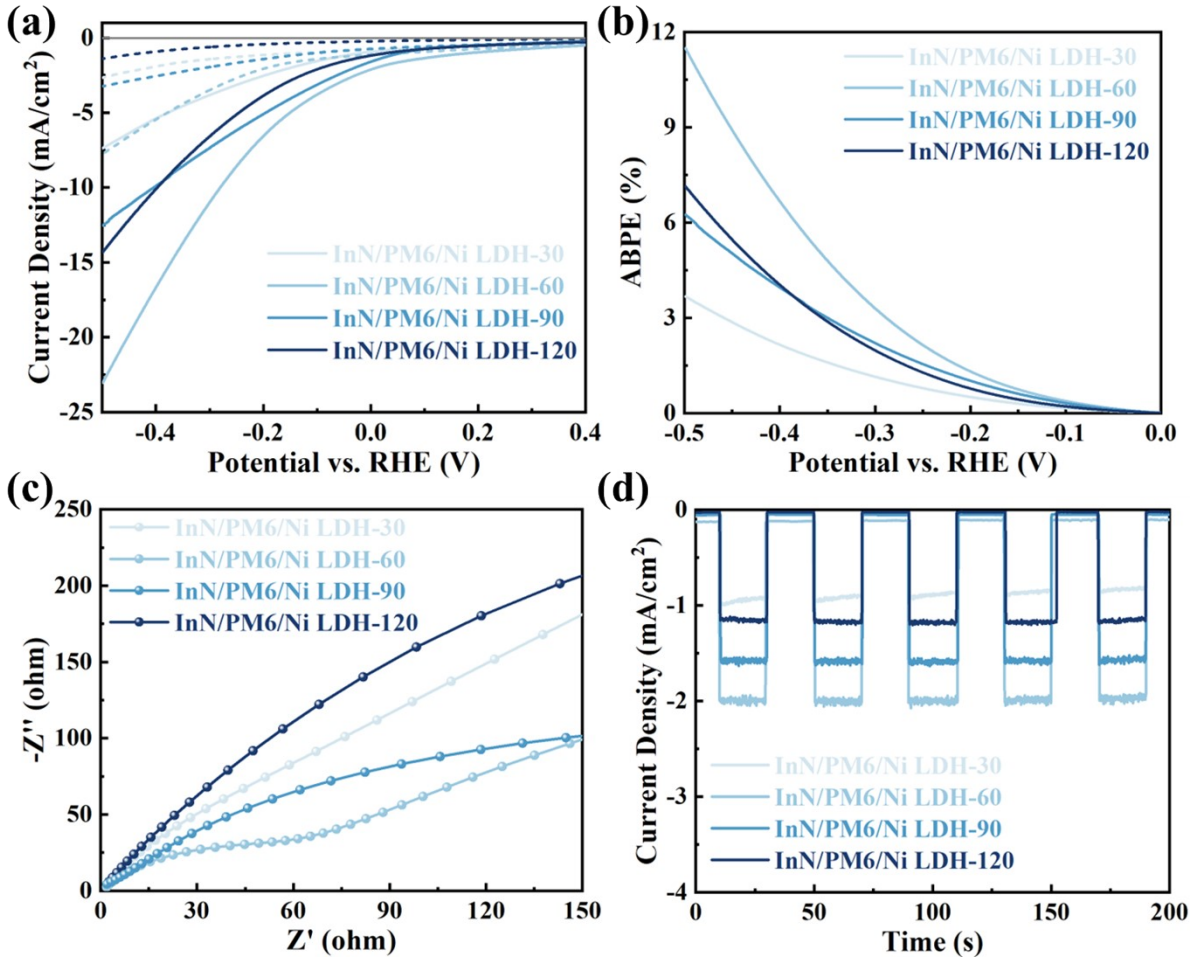

Figure S16. The (a) LSV curves, (b) ABPE curves, (c) EIS spectra, and (d) chopped J-t curves of InN/PM6/Ni LDH photocathodes with varying electrodeposition times.

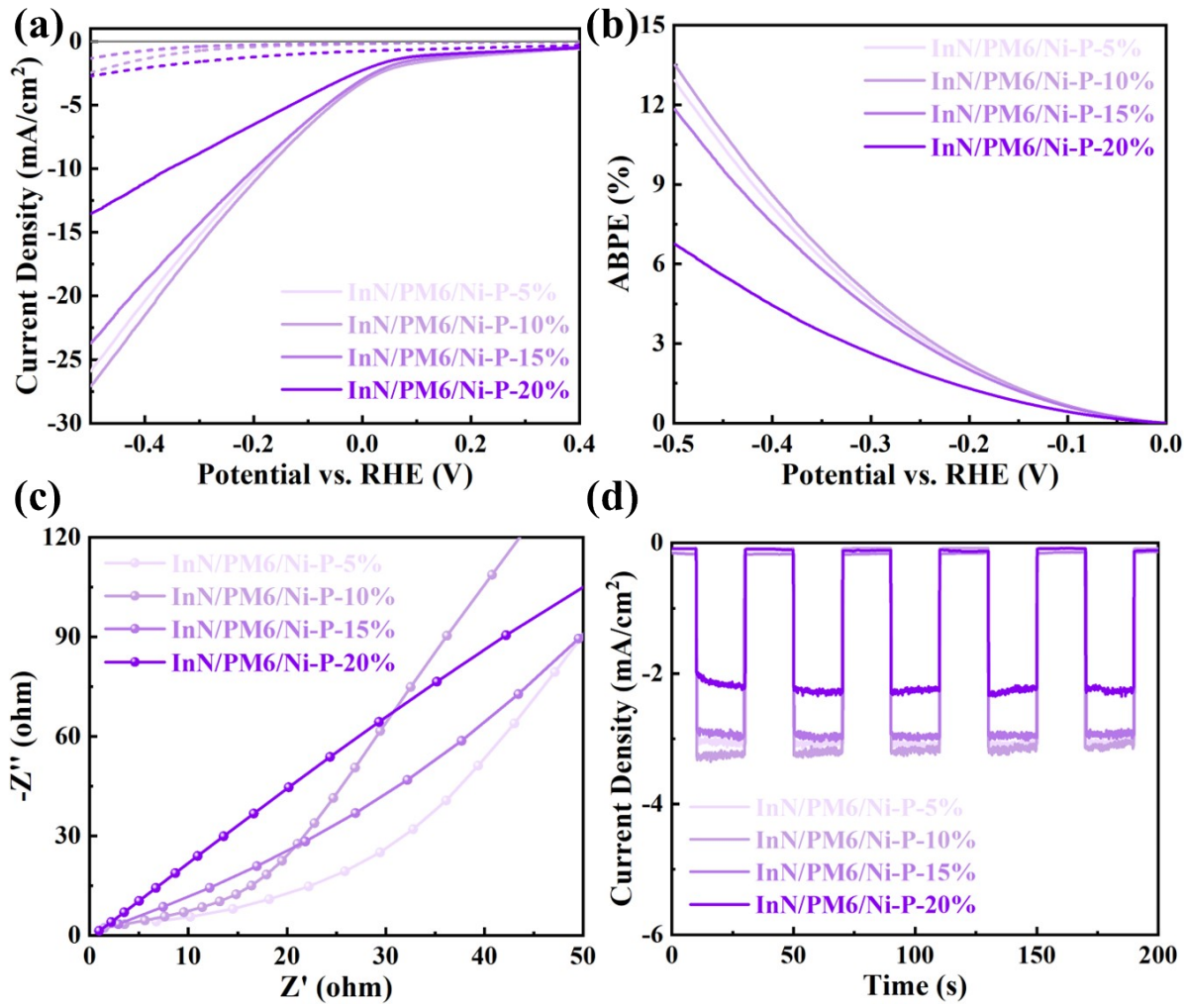

Figure S17. The (a) LSV curves, (b) ABPE curves, (c) EIS spectra, and (d) chopped J-t curves of InN/PM6/Ni LDH photocathodes with varying P content percentages.

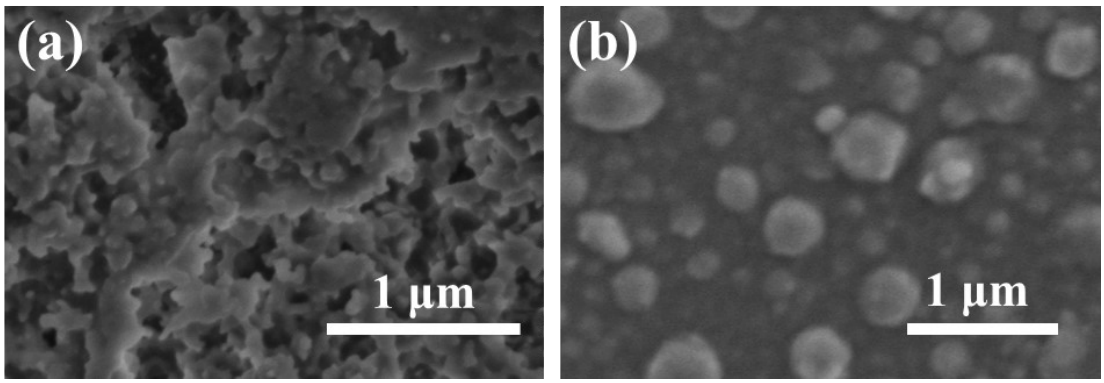

Figure S18. SEM image of (a) InN/PM6/Ni LDH and (b) InN/PM6/Ni-P photocathode after illumination under three-electrodes system.

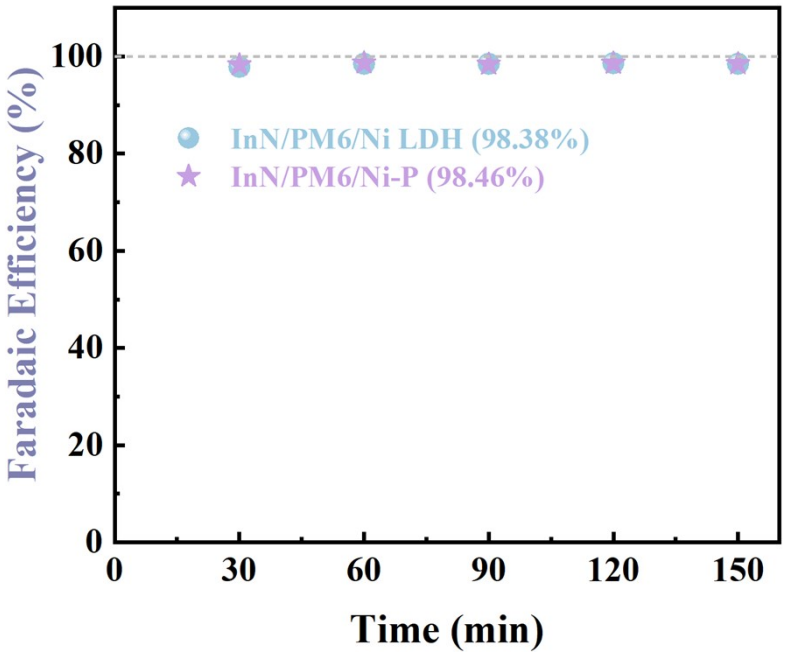

Figure S19. The FE-t curves of InN/PM6/Ni LDH and InN/PM6/Ni-P photocathodes.

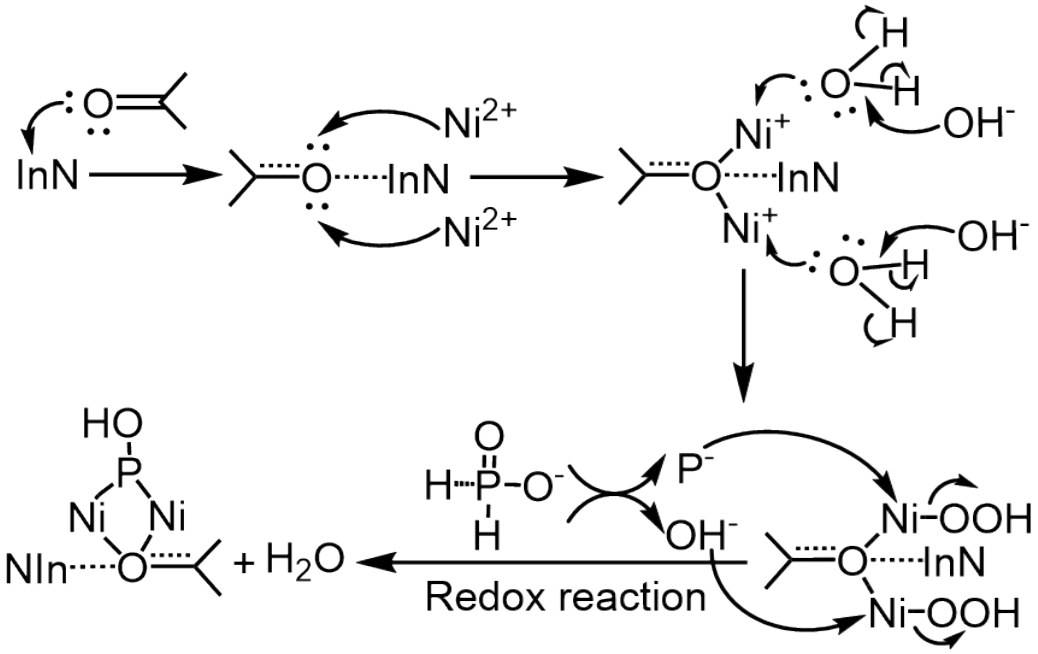

Figure S20. The reaction mechanism of in-situ preparation of Ni LDH on InN NRs promoted by carbonyl group (C=O), and the subsequent electrochemical reconstruction mechanism.

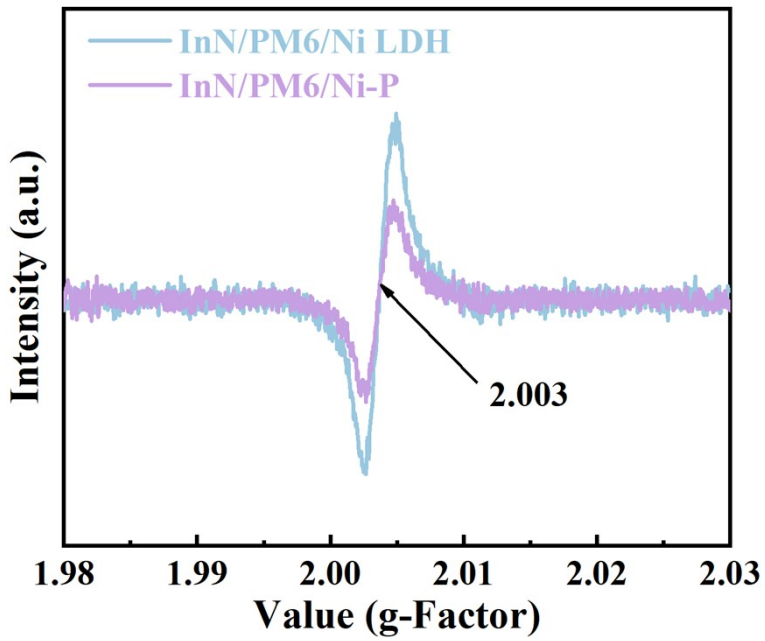

Figure S21. EPR spectra of O_{v2}-InN/PM6/Ni LDH and InN/PM6/Ni-P hybrid.

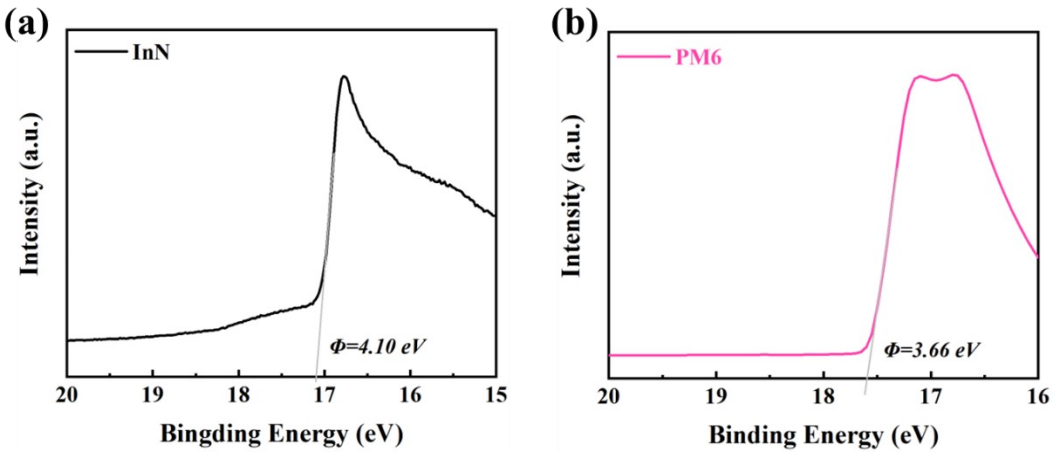

Figure S22. The UPS spectra of (a) InN and (b) PM6.

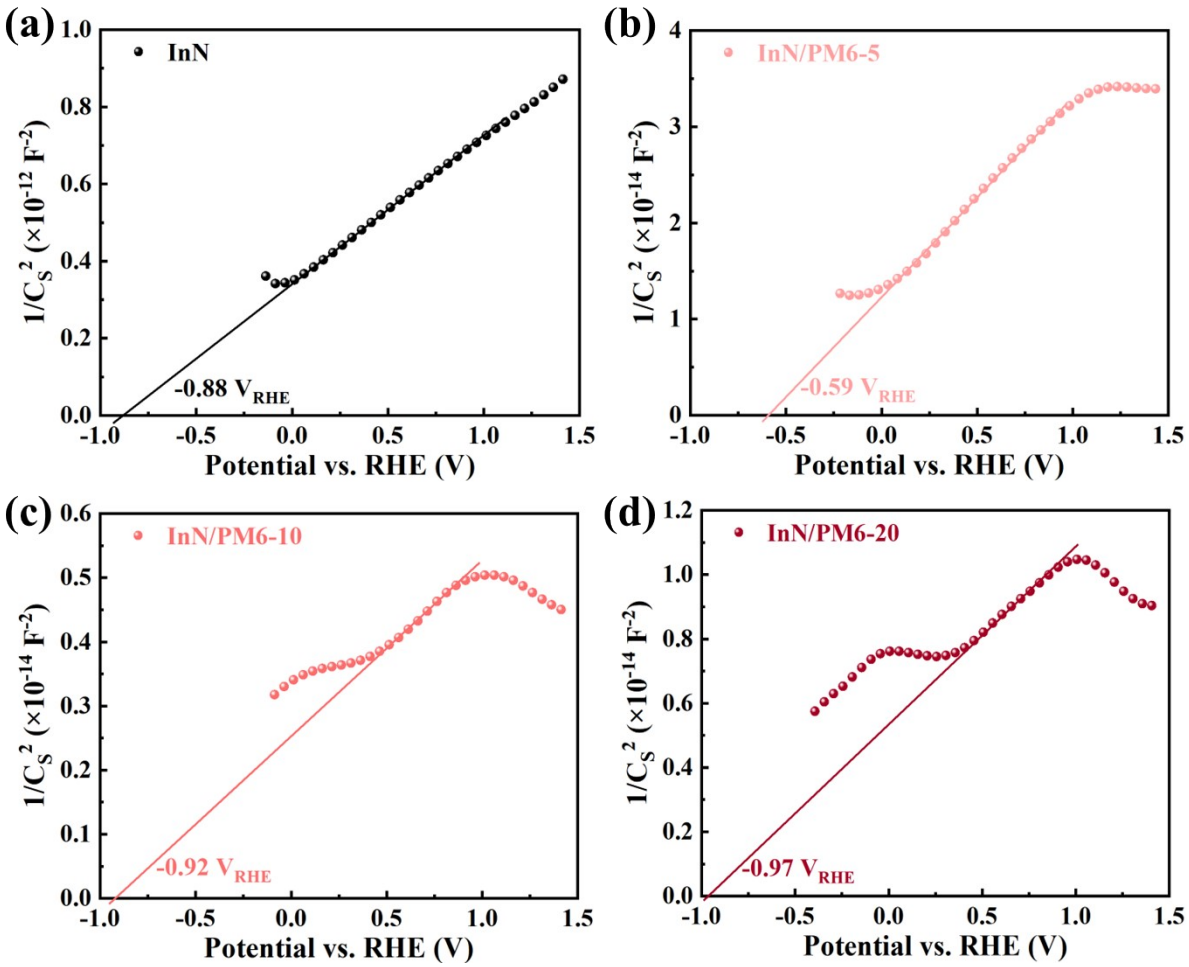

Figure S23. Mott Schottky plots of the photocathodes measured in the dark. (a) InN, (b-d) InN/PM6 photocathodes with varying mass concentrations.

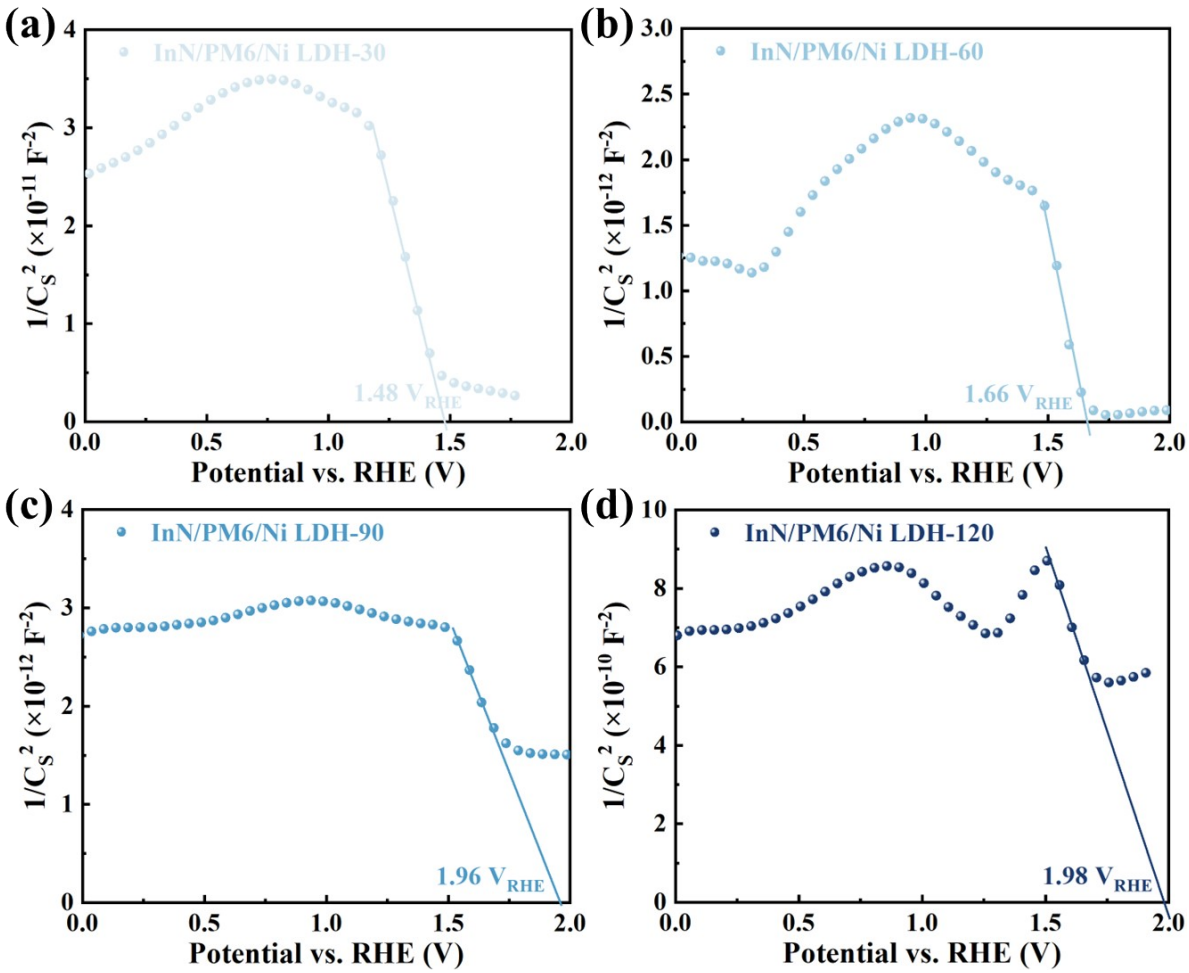

Figure S24. Mott-Schottky plots of the InN/PM6/Ni LDH photocathodes with varying electrodeposition times measured in the dark.

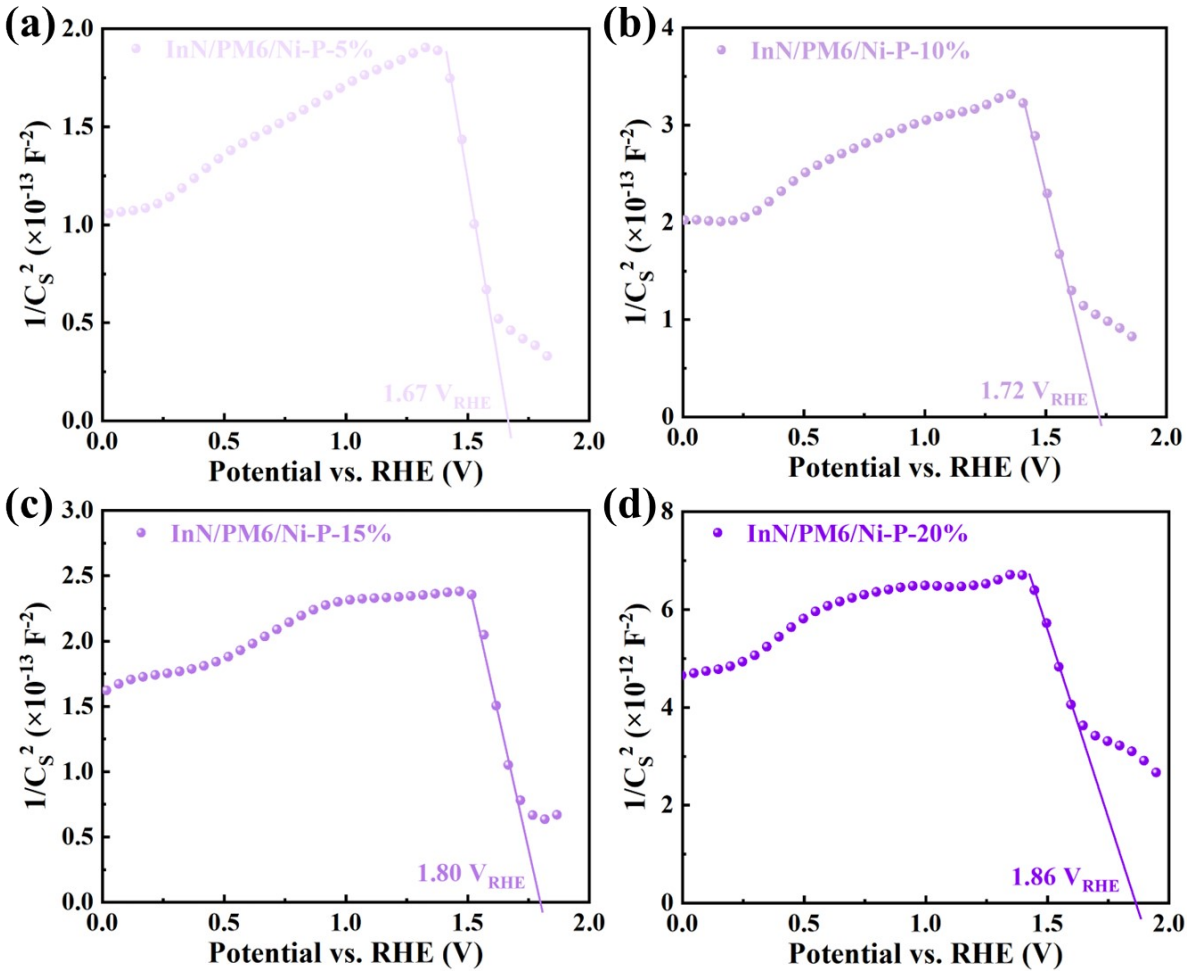

Figure S25. Mott-Schottky plots of the InN/PM6/Ni-P photocathodes with varying P content percentages measured in the dark.

Table S1. Summary of the PEC performance of InN-based heterojunction photoelectrodes under illumination of 100 mW cm^{-2} with AM 1.5G filter.

Photoelectrode	Electrolyte	Photocurrent Density (mA/cm^2)	H_2 evolution rate (μmol/h)	STH efficiency (%)	Reference
InN/PM6/Ni LDH-60	0.1 M KOH	-2.11 (0 V_{RHE})	35.76	2.41	This work
InN/PM6/Ni-P-10%	0.1 M KOH	-3.24 (0 V_{RHE})	42.42	3.11	This work
In_2O_3@InN/$ZnIn_2S_4$	0.25 M Na_2SO_3 0.35 M Na_2S	-	5.5	-	Ref. [10]
InGaN/GaN	1 M H_2SO_4	-0.36 (0 V_{RHE})	100	-	Ref. [11]
InGaN/Si	0.5 M H_2SO_4	-9.74 (0.3 V_{RHE})	3.4	-	Ref. [12]
InN@C	0.8 M $KHCO_3$ 0.2 M K_2CO_3	-1.00 (-0.6 V_{RHE})	-	-	Ref. [13]
InN/In_2O_3	0.1 M PBS	0.966 (1.0 $V_{Ag/AgCl}$)	-	-	Ref. [14]
Ni-doped InN/GaZnON	0.5 M Na_2SO_4	-	2.33	-	Ref. [15]
InN NWs	1 M NaOH	0.04 (1.23 V_{RHE})	-	-	Ref. [16]
InN/ZnO	0.1 M Na_2SO_4	0.009 (1.23 V_{RHE})	0.56	-	Ref. [17]
ZnO:InN	0.5 M Na_2SO_4	4.43 (1.23 V_{RHE})	0.012	-	Ref. [18]
InGaN/Cu_2O	0.5 M Na_2SO_4	6.48 (1.23 V_{RHE})	-	-	Ref. [19]

Table S2. V_{fb} and N_d values estimated from the slopes of M-S plots.

Photocathodes	V_{fb} (V_{RHE})	slopes	N_d (cm^{-3})
InN	-0.88	3.87×10^{-11}	1.82×10^{20}
InN/PM6-5	-0.59	2.07×10^{-14}	3.41×10^{17}
InN/PM6-10	-0.92	2.74×10^{-14}	2.58×10^{17}
InN/PM6-20	-0.97	5.51×10^{-14}	1.28×10^{17}
InN/PM6/Ni LDH-30	1.48	-1.02×10^{-10}	6.92×10^{20}
InN/PM6/Ni LDH-60	1.66	-9.17×10^{-12}	7.70×10^{19}
InN/PM6/Ni LDH-90	1.96	-6.40×10^{-12}	1.10×10^{20}
InN/PM6/Ni LDH-120	1.98	-1.90×10^{-9}	3.72×10^{21}
InN/PM6/Ni-P-5%	1.67	-7.29×10^{-13}	9.68×10^{18}
InN/PM6/Ni-P-10%	1.72	-1.06×10^{-12}	6.66×10^{20}
InN/PM6/Ni-P-15%	1.80	-8.18×10^{-13}	8.63×10^{18}
InN/PM6/Ni-P-20%	1.86	-1.54×10^{-11}	4.58×10^{21}

Table S3. PV parameters of the GaAs/CNT/WO_3 heterojunction solar cells with different GO load

Solar cell	Voc (V)	Jsc (mA/cm^2)	FF (%)	PCE (%)
GaAs/CNT/WO_3	0.787	27.89	69.46	14.40 (14.41 ± 0.12)
GaAs/CNTGO1/WO_3	0.791	28.04	71.32	14.94 (14.88 ± 0.20)
GaAs/CNTGO2/WO_3	0.793	30.85	70.22	16.21 (16.05 ± 0.18)
GaAs/CNTGO5/WO_3	0.790	30.86	69.17	15.91 (15.83 ± 0.21)
GaAs/CNTGO10/WO_3	0.788	28.02	69.73	14.55 (14.43 ± 0.25)

REFERENCES

1. J. Lin, Y. F. Yu, Z. J. Zhang, F. L. Gao, S. Liu, W. L. Wang and G. Q. Li, *Adv. Funct. Mater.*, 2020, **30**, 11.
2. Y. T. Mo, S. H. Xie, T. Y. Huang, R. B. Liao, J. H. Hu, F. S. Chen, W. T. Huang, J. F. Zhang, J. Chen, L. J. Sun, W. L. Wang and G. Q. Li, *Chem. Eng. J.*, 2025, **519**, 8.
3. Y. X. Chen, X. L. Li, H. Yang and Y. C. Huang, *Small*, 2024, **20**, 11.
4. Y. C. Hu, Z. T. Shi, X. L. Ren, Y. X. Cao, G. H. Xiao, D. W. Huang and F. Jiang, *Adv. Energy Mater.*, 2024, **14**, 9.
5. J. Lin, W. L. Wang and G. Q. Li, *Adv. Funct. Mater.*, 2020, **30**, 20.
6. X. L. Ma, Y. J. Zhou, S. Zhang, W. L. Lei, Y. M. Zhao and C. S. Shan, *Small*, 2025, **21**, 10.
7. J. Z. Liao, M. Y. Xue, Y. K. Bao, Z. T. Wu, H. Zhang, P. Li, X. Xu and S. Duo, *ACS Appl. Energ. Mater.*, 2023, **6**, 4683-4692.
8. L. L. Gao, F. Li, H. G. Hu, X. F. Long, N. Xu, Y. P. Hu, S. Q. Wei, C. L. Wang, J. T. Ma and J. Jin, *ChemSusChem*, 2018, **11**, 2502-2509.
9. Z. Z. Xu, S. G. Zhang, J. H. Liang, J. Lin, Y. F. Yu, R. Z. Li, F. L. Gao and G. Q. Li, *J. Power Sources*, 2019, **419**, 65-71.
10. H. H. Zhang, H. J. Gu, X. H. Wang, L. F. Li, J. H. Zhang, S. Y. Chang and W. L. Dai, *J. Colloid Interface Sci.*, 2022, **622**, 539-548.
11. H. F. Zhang, M. Ebaid, J. Tan, G. Y. Liu, J. W. Min, T. K. Ng and B. S. Ooi, *Opt. Express*, 2019, **27**, A81-A91.
12. S. Vanka, B. W. Zhou, R. A. Awni, Z. N. Song, F. A. Chowdhury, X. D. Liu, H. Hajibabaei, W. Shi, Y. X. Xiao, I. A. Navid, A. Pandey, R. Chen, G. A. Botton, T. W. Hamann, D. W. Wang, Y. F. Yan and Z. T. Mi, *ACS Energy Lett.*, 2020, **5**, 3741-3751.
13. J. F. Chen, X. Y. Zhu, Y. Yu, T. Huang, K. F. Zhang, Q. Q. Luo, S. Gao and J. L. Yang, *Appl. Catal. B-Environ. Energy*, 2025, **361**, 11.
14. A. Saroni, M. Alizadeh, S. A. Rahman, W. Meevasana and B. T. Goh, *J. Power Sources*, 2020, **480**, 10.
15. X. L. Hou, S. H. Jiang, Y. Li, J. R. Xiao and Y. D. Li, *Int. J. Hydrogen Energy*, 2015, **40**, 15448-15453.
16. J. Kamimura, P. Bogdanoff, M. Ramsteiner, L. Geelhaar and H. Riechert, *Semicond. Sci. Technol.*, 2016, **31**, 6.
17. H. Q. Liu, X. Z. Ma, Z. X. Chen, Q. G. Li, Z. Y. Lin, H. Liu, L. Y. Zhao and S. Chu, *Small*, 2018, **14**, 9.
18. S. S. Menon, H. Y. Hafeez, B. Gupta, K. Baskar, G. Bhalerao, S. Hussain, B. Neppolian and S. Singh, *Renew. Energy*, 2019, **141**, 760-769.
19. J. Lin, Z. J. Zhang, J. X. Chai, B. Cao, X. Deng, W. L. Wang, X. J. Liu and G. Q. Li, *Small*, 2021, **17**, 10.